Journal of Materials Science & Technology 34 (2018) 1337–1343

Contents lists available at ScienceDirect

Journal of Materials Science & Technology

journal homepage: www.jmst.org

High-temperature phase transition behavior and magnetocaloric effect in a sub-rapidly solidified La–Fe–Si plate produced by centrifugal casting

Zhishuai Xu[a,b], Yuting Dai[a], Yue Fang[a], Zhiping Luo[c], Ke Han[d], Changjiang Song[b], Qijie Zhai[b], Hongxing Zheng[a,b,*]

[a] Laboratory for Microstructures, Shanghai University, Shanghai 200444, China
[b] State Key Laboratory of Advanced Special Steel, Shanghai University, Shanghai 200444, China
[c] Department of Chemistry and Physics, Fayetteville State University, Fayetteville, NC 28301, USA
[d] National High Magnetic Field Laboratory, Florida State University, Tallahassee, FL 32310, USA

ARTICLE INFO

Article history:
Received 13 September 2017
Received in revised form 19 October 2017
Accepted 6 November 2017
Available online 10 November 2017

Keywords:
La–Fe–Si
Magnetocaloric effect
Rapid solidification
Centrifugal casting
Phase transition

ABSTRACT

A sub-rapidly solidified $LaFe_{11.6}Si_{1.4}$ plate was fabricated directly from liquid by centrifugal casting method. The phase constitution, microstructure and magnetocaloric effect were investigated using backscatter scanning electron microscopy, X-ray diffraction, differential scanning calorimetry and physical property measurement system. When the plate was annealed at 1373 K, $\tau1$ phase was formed by a solid-state peritectoid reaction. A first-order magnetic phase transition occurred in the vicinity of 188 K, and the effective refrigeration capacities reached 203.5 J/kg and 209.7 J/kg in plates annealed for 1 h and 3 h, respectively, under a magnetic field change of 3 T. It is suggested that centrifugal casting may become a new approach to prepare high-performance La–Fe–Si magnetocaloric plates for practical applications, which could largely accelerate the formation of $\tau1$ phase during high-temperature heat-treatment process due to refined and homogeneous honeycombed microstructure.

© 2017 Published by Elsevier Ltd on behalf of The editorial office of Journal of Materials Science & Technology.

1. Introduction

Magnetic refrigeration has been widely utilized in low-temperature region since 1980s [1]. With regard to the applications near room temperature, Brown developed a magnetic heat pump using heavy rare-earth Gd metal as magnetocaloric materials in 1976 [2]; however, it did not attract much attention until Gschneidner and Pecharsky discovered giant magnetocaloric effect (GMCE) of $Gd_5(Si,Ge)_4$ in 1997, which exhibited a higher magnetic entropy change (ΔS_M) at least doubled that of Gd [3]. Compared with the conventional vapor compression/expansion system, magnetic refrigeration can be up to 30% more energy-efficient; furthermore, it makes less noise due to the absence of a compressor and makes use of water-based coolants instead of gaseous refrigerants, and therefore it has been strongly pushed during the past two decades [4]. Several countries, including US [5], Japan [6], France [7], China [8] and Canada [9], developed various types (rotary/reciprocating) of room-temperature magnetic refrigerators. Recently, Haier of China, along with Astronautics Corporation of America and BASF of Germany, presented a prototype of a magnetocaloric wine cooler in 2015 [10]. Cooltech Applications of France also announced their commercial magnetic cooling system in 2016 [11].

Among three constituent parts in a room-temperature magnetic cooling system, both magnet (superconducting/permanent) and heat exchanger are relatively mature, whereas the bottleneck lies in the exploration of low-cost super-performance magnetocaloric materials. Although over 100 kinds of magnetocaloric materials have been reported, a few of them are suitable for practical use [12–15]. From the viewpoint of price/performance ratio, La–Fe–Si system is considered to be one of the most potential candidates [16]. In case of La–Fe–Si, the main challenge is how to obtain high-proportional $NaZn_{13}$-type $La(Fe,Si)_{13}$ (1:13, $\tau1$) phase. Niitsu and Kainuma reported that neither α(Fe) nor LaFeSi (1:1:1) phases could be eliminated in arc-melted $LaFe_{11.6}Si_{1.4}$ bulk alloy even annealed at 1173 K for 45 days, because of the abrupt declination of the solidus line of $\tau1$ phase and the low atomic diffusivity. An increase in temperature to 1373 K for 5 days was needed to obtain a pure $\tau1$ phase [17]. Although melt spinning technique is helpful to promote the formation of $\tau1$ phase, the resultant ribbons

* Corresponding author at: Laboratory for Microstructures, Shanghai University, Shanghai, 200444, China.
E-mail address: hxzheng@shu.edu.cn (H. Zheng).

https://doi.org/10.1016/j.jmst.2017.11.023
1005-0302/© 2017 Published by Elsevier Ltd on behalf of The editorial office of Journal of Materials Science & Technology.

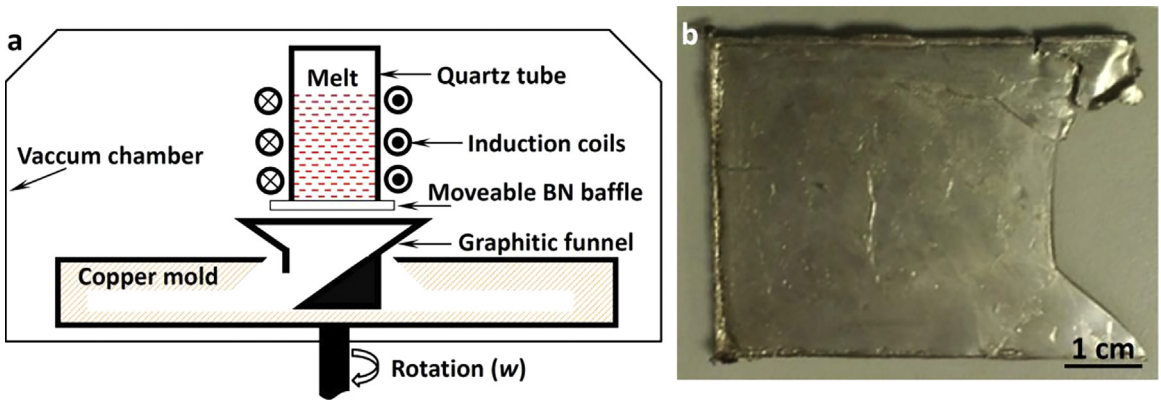

Fig. 1. Schematic diagram of the centrifugal casting setup (a) and image of the produced plate (b).

have to be embedded into polymer matrix for practical applications, and it is inevitable to arise more unexpected problems, such as interfacial bonding and thermal conductivity [18,19]. Besides, the intrinsic brittleness of $\tau 1$ phase largely restricted its production and applications, and how to fabricate La–Fe–Si plates without complex machining is another challenge [20–22].

In the present work, we firstly attempted to prepare a sub-rapidly solidified La–Fe–Si plate by employing centrifugal casting method [23], and investigated the phase constitution, microstructure and magnetocaloric effect. The main objective is to explore the feasibility of centrifugal casting for the fabrication of La–Fe–Si plates.

2. Materials and experiments

A button $LaFe_{11.6}Si_{1.4}$ (at.%) ingot was first arc-melted from pure La (99.9 wt%), Fe (99.99 wt%) and Si (99.999 wt%) in argon gas atmosphere. The plate with a dimension of ~60 mm × 40 mm × 2.5 mm was fabricated using a customer-designed centrifugal casting setup, as illustrated in Fig. 1. The chamber was vacuumed and then filled with high-purity argon for protection. When the button ingot was remelted by high-frequency induction heating, the melt was poured into a high-speed rotary centrifugal copper mold (w = 3000 rpm) through the graphitic funnel. The cooling rate was estimated to be about 5000 K/s. Two samples were cut from the produced plate, sealed in quartz tubes and annealed at 1373 K for 1 h and 3 h, respectively, followed by water quenching. Hereinafter the as-cast plate and two annealed samples for 1 h and 3 h were referred to as RP0, RP1 and RP3, respectively. One more sample was annealed at 1423 K for 1 h for comparison in the present work.

Microstructural observations were performed using a backscatter scanning electron microscopy (SEM, JSM-6700) equipped with an energy-dispersive spectrometry (EDS). Topological morphology was obtained by 3D roughness reconstruction method. X-ray diffraction (XRD, DLMAX-2500) with Cu K_α radiation was employed to detect the phase and crystal structure at a scanning rate of 1°/min. High-temperature differential scanning calorimetric measurement (DSC, NETZSCH 404 F3) was carried out at a heating/cooling rate of 20 K/min. Magnetic properties were conducted on a physical property measurement system (Quantum Design PPMS-9) under a maximum magnetic field up to 3 T.

3. Results and discussion

3.1. Phase and microstructure

Backscatter SEM image of arc-melted $LaFe_{11.6}Si_{1.4}$ alloy is presented in Fig. 2, where one can see coarse dendrites as previously

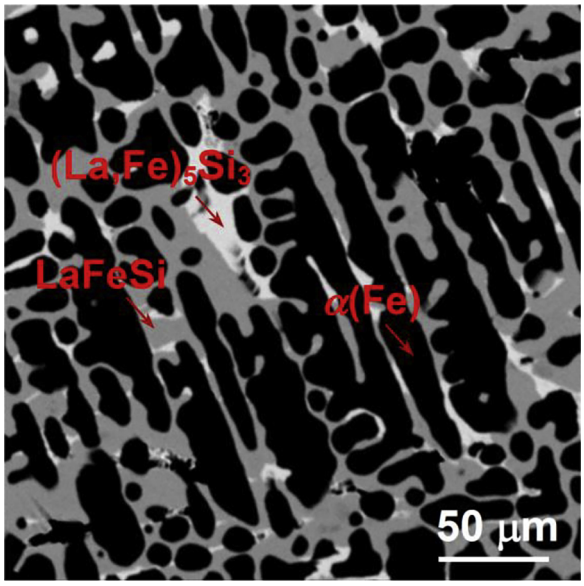

Fig. 2. Backscatter SEM image of arc-melted $LaFe_{11.6}Si_{1.4}$ alloy.

reported [24]. The SEM image of $LaFe_{11.6}Si_{1.4}$ as-cast plate (RP0) shows refined and homogeneous honeycombed microstructure (Fig. 3(a)). EDS analyses reveal that the black and white areas represent α(Fe) and LaFeSi phases, respectively. A few La-rich $(La,Fe)_5Si_3$ (5:3) phase close to shrinkage cavities can be found (Fig. 3(b)), as shown in the topological morphology in Fig. 3(c), indicating that the $(La,Fe)_5Si_3$ phase is a product of residual liquid phase during rapid cooling. After annealing at 1373 K for 1 h, the contents of both α(Fe) and LaFeSi phases decrease dramatically. Isolated α(Fe) and slightly agglomerated LaFeSi phases distribute in the grey $\tau 1$ matrix (Fig. 3(d)). The $\tau 1$ phase significantly increases from 76.1 vol.% to 89.8 vol.% after annealing for 3 h (Fig. 3(e)). The volume fractions of the phases were determined from at least 10 SEM images. The average chemical composition and volume fraction for α(Fe), LaFeSi and $\tau 1$ phases are listed in Table 1.

XRD patterns show that in the RP0, the major diffraction peak is from α(Fe) phase at 43.9° (Fig. 4(a)). After annealing at 1373 K for 1 h (RP1), the XRD intensity from $\tau 1$ phase increases while the intensity from LaFeSi phase is reduced. After annealing at 1373 K for 3 h (RP3), the intensity of α(Fe) main peak at 43.9° decreases noticeably and the peaks from $\tau 1$ phase dominate the pattern [25]. A few weak peaks from $(La,Fe)_5Si_3$ phase are detected in both annealed plates although it is difficult to be found in the SEM images. Diffraction peaks at 43.9° and 64.2° from α(Fe) phase in RP1 and RP3 shift towards lower angles compared with those of RP0, indicating

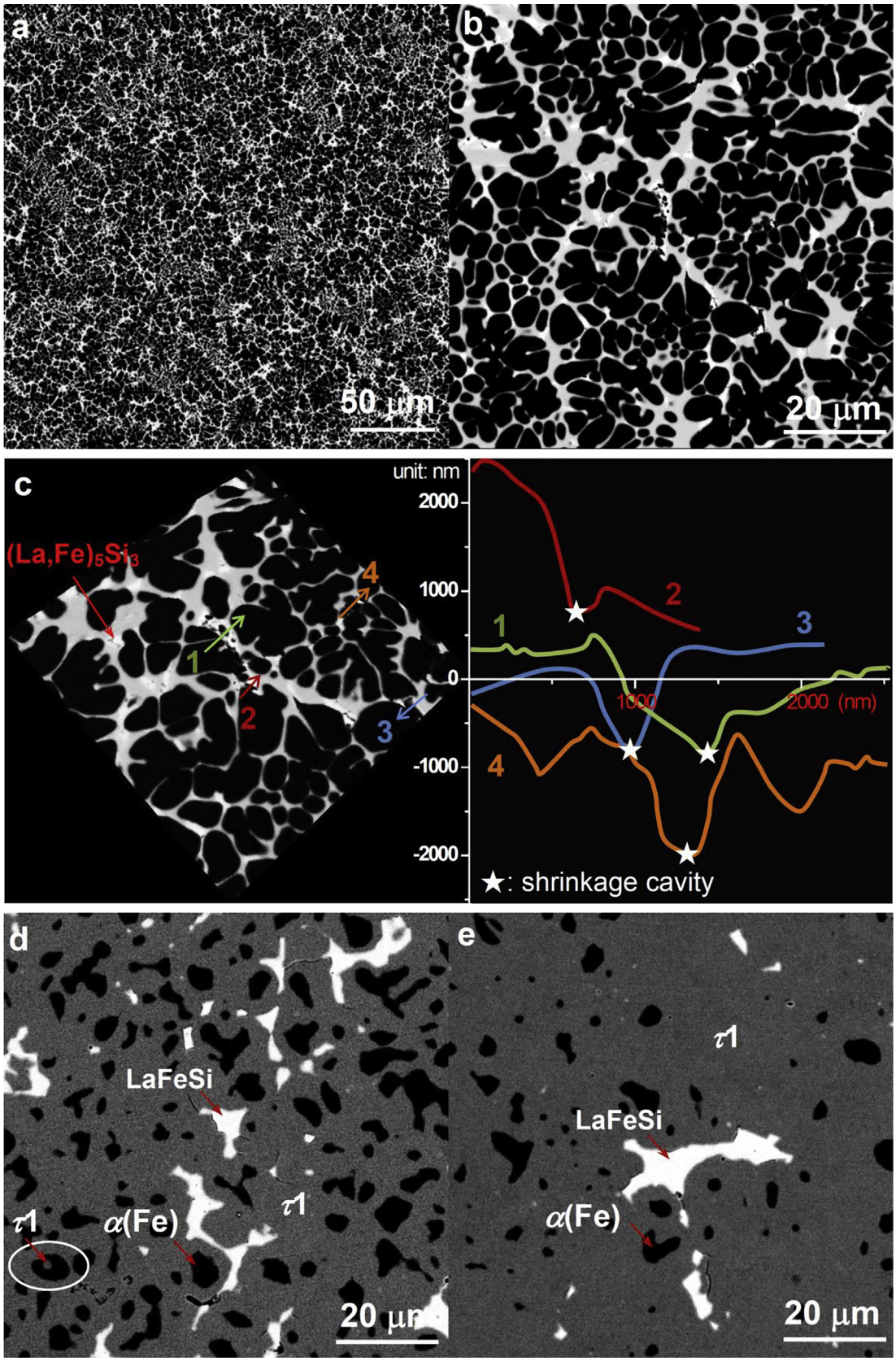

Fig. 3. Backscatter SEM images of $LaFe_{11.6}Si_{1.4}$ plates: (a, b) RP0, (d) RP1 and (e) RP3. (c) A topological morphology showing La_5Si_3 phase close to shrinkage cavities in RP0, and the curves in the right represent the depth change measured from 4 typical zones.

Table 1
Average chemical composition (at.%) and volume fraction (vol.%)[a] for each phase in the $LaFe_{11.6}Si_{1.4}$ plate.

	α(Fe)			LaFeSi				τ1			
	Fe	Si	vol.%	La	Fe	Si	vol.%	La	Fe	Si	vol.%
RP0	93.0	7.0	69.3	30.0	36.5	33.5	30.7	–	–	–	0
RP1	95.3	4.7	17.6	26.7	38.6	34.7	6.3	6.5	80.8	12.7	76.1
RP3	95.6	4.4	6.4	27.2	40.8	32.0	3.8	6.8	81.6	11.6	89.8

[a] The volume fraction was estimated from SEM images.

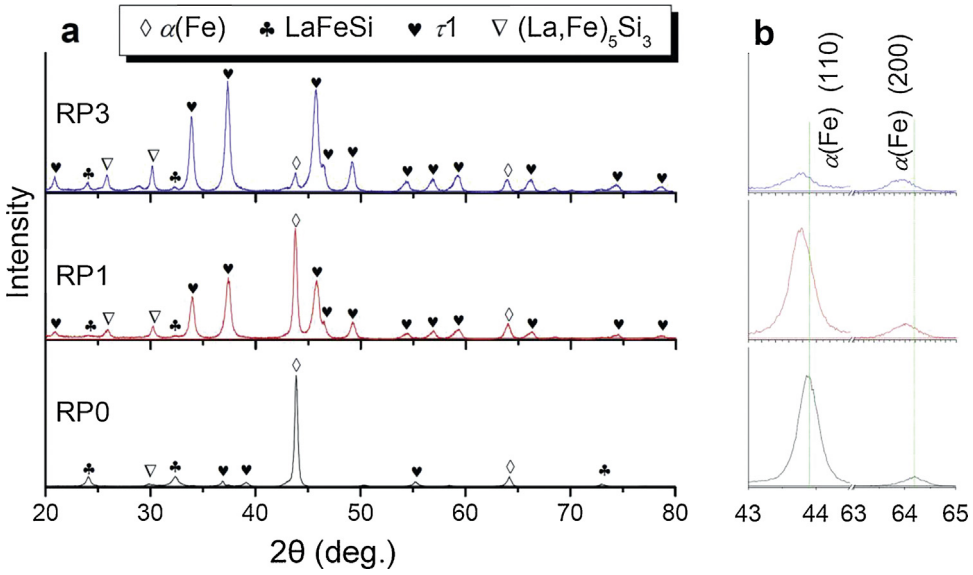

Fig. 4. XRD patterns of $LaFe_{11.6}Si_{1.4}$ plates at room temperature.

that the unit cell expands slightly in RP1 and RP3 after annealing (Fig. 4(b)). The expansion can be attributed to some smaller Si atoms desolventizing from the sub-rapidly solidified supersaturated α(Fe) phase. The shift of diffraction peaks of τ1 phase also suggests an expansion of the unit cell because of reduced Si contents after prolonged annealing (Fig. 4(a)), as confirmed by EDS in Table 1.

3.2. High-temperature phase transition behavior

In order to clarify the high-temperature phase transition behavior of sub-rapidly solidified plate, DSC measurement was conducted. Firstly, a small fluctuation at 1016 K upon heating, as circled in Fig. 5, shows the Curie temperature for the magnetic transition of α(Fe) phase, as shown in Fe–Si binary phase diagram [26]. The increase of Curie temperature (1087 K) upon cooling is attributed to less Si dissolved in the sample formed upon solidification with lower cooling rate (20 K/min) than that used for sub-rapidly solidified plate (~5000 K/s). Secondly, as for the equilibrium solidification process of La–Fe–Si, it has been commonly accepted that α(Fe) is the primary phase and τ1 is a peritectic phase [27,28]. With this in mind we can conclude that the two sharp exothermic peaks (1651 K and 1509 K) upon cooling (20 K/min) are caused by the formation of α(Fe) and τ1 phases, respectively. The corresponding endothermic peaks appearing at 1580 K and 1694 K upon heating are resulted from the melting of τ1 and α(Fe) phases, respectively, as noted in Fig. 5. Lastly, from the enlarged heat-flow heating curve between 1250 K and 1650 K, as shown in the inset, one observes peaks 1 (1400 K) and 2 (1480 K). We suggest that they correspond to the melting of LaFeSi phase and the formation of τ1 phase, respectively. Based on the model, we conclude that the

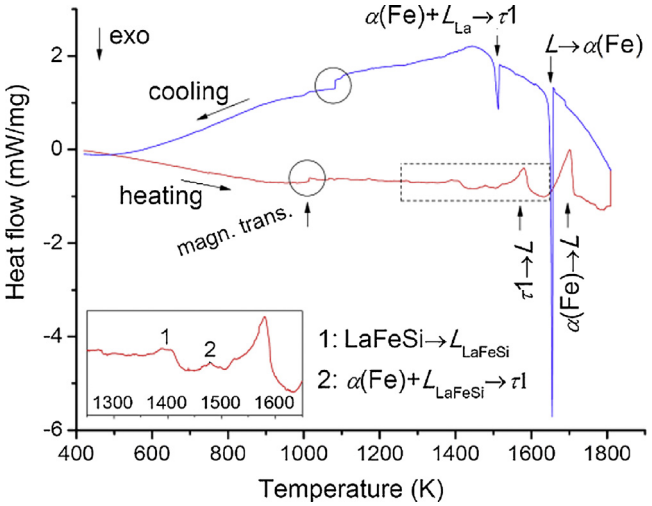

Fig. 5. DSC curve of the sub-rapidly solidified $LaFe_{11.6}Si_{1.4}$ plate (20 K/min).

1373 K heat treatment of the present work was fully completed within solid-phase stage.

On the formation of τ1 phase during solid-state heat-treatment stage, Fu et al. proposed that the τ1 phase formed through a eutectoid reaction ($LaFeSi \rightarrow \tau 1 + La_5Si_3$) at 1445 K in the $LaFe_{11.5}Si_{1.5}$ based on DSC measurement [29]. Liu et al. also proposed that it may be associated with a certain eutectoid reaction based on a lamellar structure feature that they observed in annealed $LaFe_{11.6}Si_{1.4}$ at 1323 K; however, they did not find La_5Si_3 (5:3) inside the transition layer [30]. As shown in Fig. 3(b and c), we proposed the $(La,Fe)_5Si_3$ phase is resulted from the residual liquid phase during rapid cooling. It is pronely considered that the τ1 phase is formed

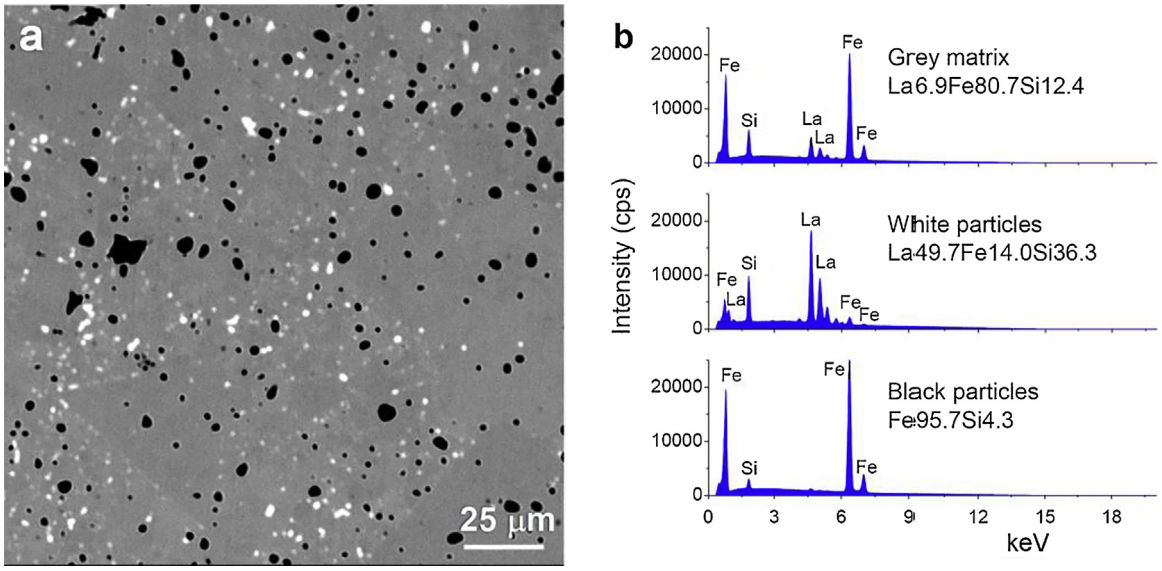

Fig. 6. (a) Backscatter SEM image of sub-rapidly solidified $LaFe_{11.6}Si_{1.4}$ plate annealed at 1423 K for 1 h. (b) EDS measurements taken from the grey matrix, white and black particles, showing $\tau1$, $(La,Fe)_5Si_3$ and α(Fe) phases, respectively. The average chemical compositions (at.%) for each phase are added on the EDS spectra.

through peritectoid interdiffusion between α(Fe) and LaFeSi phases based on the following three facts: (1) the annealing temperature of 1373 K is very close to the melting point of LaFeSi phase (1400 K); (2) one can observe that a few $\tau1$ phase was surrounded by α(Fe), as marked by a white oval circle in Fig. 3(d); (3) LaFeSi phase completely vanished when the plate was annealed at 1423 K for 1 h (~91 vol.% $\tau1$ phase), just above the peak 1 (1400 K), as shown in Fig. 6, where all the white particles are determined to be $(La,Fe)_5Si_3$ phase by EDS. Compared with the conventional bulk alloys, the diffusion process at 1373 K in the sub-rapidly solidified plate was strikingly accelerated due to refined and homogeneous microstructure.

3.3. Magnetic transition and magnetocaloric effect

The field cooling and field heating *M-T* curves were measured under a low magnetic field of 0.05 T, as shown in Fig. 7. Both RP1 and RP3 show a similar trend. A sudden drop of magnetization occurs upon heating, corresponding to a ferromagnetic-paramagnetic transition [31]. Whereas upon cooling, the reverse phase transition happens. The Curie temperature is defined as the minimum in d*M*/d*T* value, see the insets in Fig. 7, which are 187.6 K for RP1 and 188.8 K for RP3 upon heating, respectively. The magnetization above the Curie temperature of RP3 is smaller than that of RP1 owing to less residual α(Fe) phase [32]. The temperature hysteresis of magnetic transition upon heating and cooling is about 4.5 K and 7.7 K, respectively. Several selected isothermal magnetization *M-H* curves around the Curie temperature are shown in Fig. 8(a and b), which were measured under a maximum magnetic field change of 3 T with a temperature interval of 3 K. The samples were firstly cooled down to 150 K with zero-field, and then heated up to 225 K. The stripped areas marked in Fig. 8(a and b) stand for the hysteretic losses. Fig. 8(c and d) is the Arrot plots (M^2 versus μ_0H/M) [33] calculated from the *M-H* curves, where inflection points (S-shape) around the Curie temperature are observed in both RP1 and RP3. These features (hysteretic loss and inflection point) are strong evidences for the first-order phase transition [34]. The increasing and decreasing magnetic field processes are indicated by arrows.

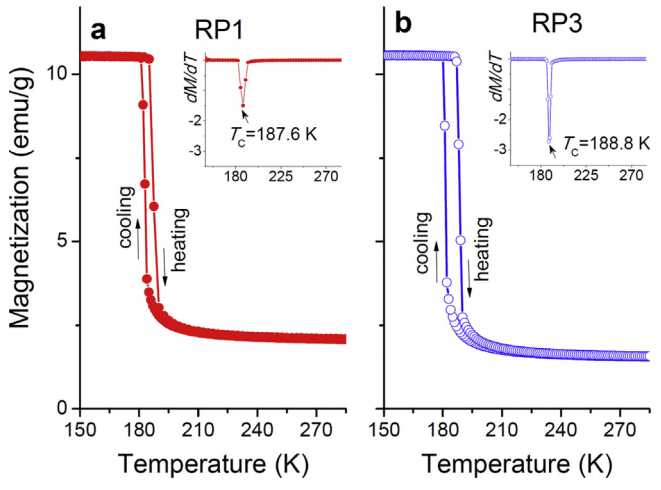

Fig. 7. Magnetization curves of annealed $LaFe_{11.6}Si_{1.4}$ plates upon heating and cooling under a magnetic field of 0.05 T. Insets are the d*M*/d*T* plots upon heating.

According to the *M-H* curves, magnetic entropy change (ΔS_M) can be estimated using the Maxwell equation [35], as shown in Fig. 9. In the work, the magneotcaloric effect under the magnetic field change of 3 T was focused. One can find that $\Delta S_M(T,H)$ peaks have asymmetrical broad phenomena to higher temperature. The maximum $|\Delta S_M|$ values are 20.9 J/(kg K) for RP1 and 22.2 J/(kg K) for RP3, respectively, under a magnetic field change of 3 T. After subtracting the average hysteretic losses resulted from the first-order phase transition, the effective refrigeration capacities (RC_{eff}) [36] reach 203.5 J/kg and 209.7 J/kg, respectively. Compared with conventional long-term annealed $LaFe_{11.6}Si_{1.4}$ bulk alloy [30,37], the sub-rapidly solidified plate demonstrates excellent refrigeration capacity even annealed at 1373 K for 1 h. It is interesting to find that RP1 still contains about 17.6 vol.% α(Fe) phase, which has been proved to be beneficial to the mechanical properties [38]. Therefore, our work provides a feasible approach to produce high-strength (with better functional fatigue) giant magnetocaloric La–Fe–Si plates. In terms of future research, it is worthy to explore its magnetic/mechanical properties with dual-phase (α(Fe) + $\tau1$) coupled microstructure.

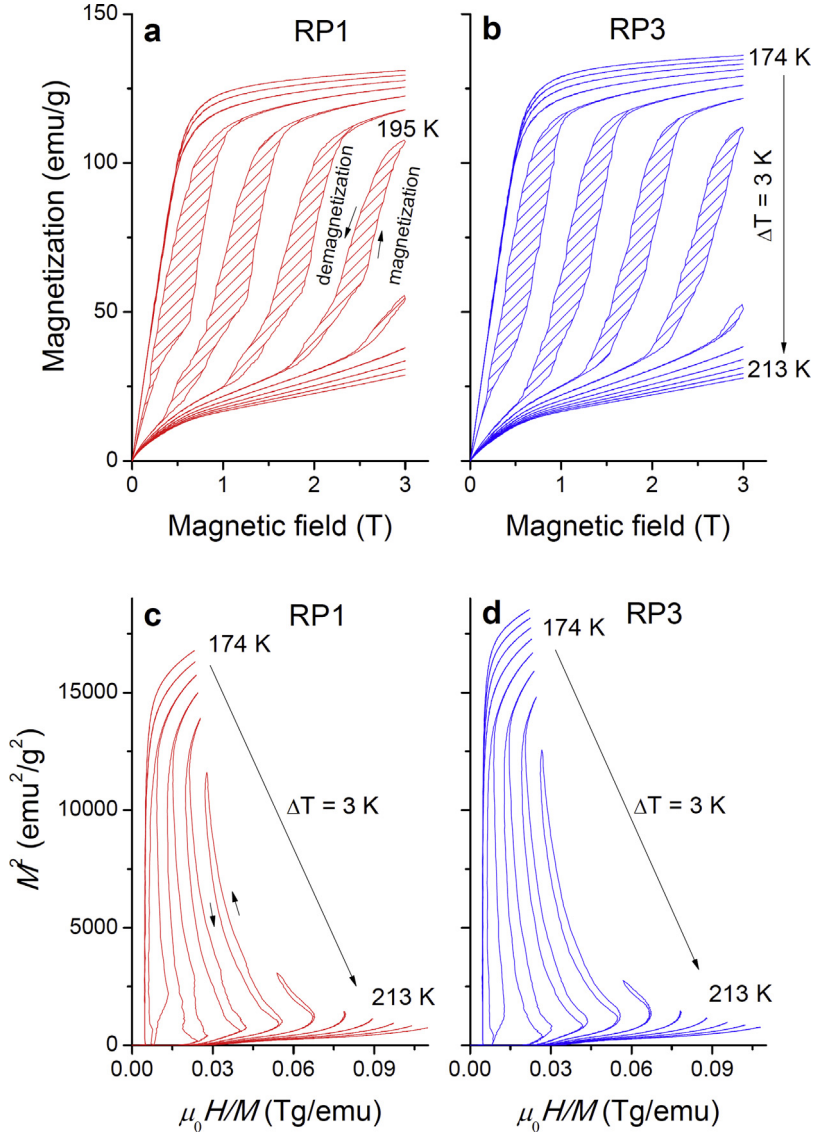

Fig. 8. (a, b) Selected isothermal magnetization curves under a magnetic field change of 3 T and (c, d) the Arrot plots around the magnetic transition of annealed $LaFe_{11.6}Si_{1.4}$ plates.

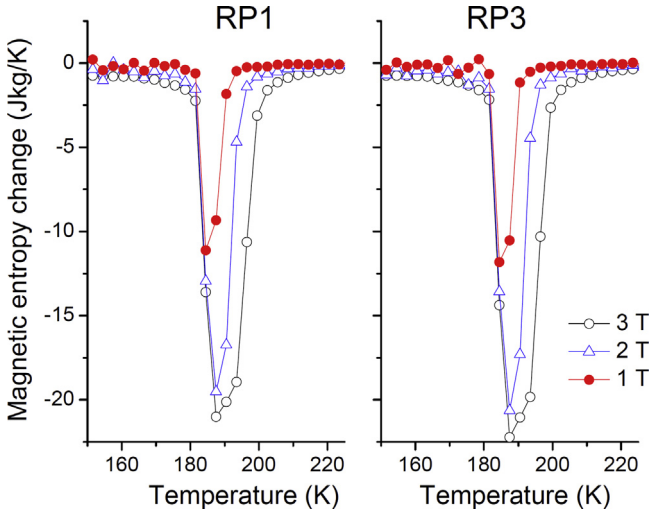

Fig. 9. Magnetic entropy change values as a function of temperature for annealed $LaFe_{11.6}Si_{1.4}$ plates.

4. Conclusions

We investigated the phase constitution, microstructure and magnetocaloric effect in a sub-rapidly solidified La–Fe–Si plate in the present work and the following conclusions are obtained.

(1) Centrifugal casting provides a new approach to produce La–Fe–Si magnetocaloric plates, which could strongly promote the formation of $\tau 1$ phase by refining the phase and microstructure.
(2) The $\tau 1$ phase is formed through solid-state peritectoid reaction between LaFeSi and α(Fe) phases when annealing at 1373 K for the sub-rapidly solidified $LaFe_{11.6}Si_{1.4}$ plate.
(3) Annealed $LaFe_{11.6}Si_{1.4}$ plate undergoes a first-order magnetic phase transition around 188 K, and the effective refrigeration capacities reach 203.5 J/kg and 209.7 J/kg under a magnetic field change of 3 T after annealed at 1373 K for 1 h and 3 h, respectively.

Acknowledgements

This work was financially supported by the National Natural Science Foundation of China (No. 51474144) and the Shanghai Sailing Program (No. 17YF1405900).

References

[1] K.A. Gschneidner Jr., V.K. Pecharsky, Int. J. Refrig. 31 (2008) 945–961.
[2] G.V. Brown, J. Appl. Phys. 47 (1976) 3673–3680.
[3] V.K. Pecharsky, K.A. Gschneidner Jr., Appl. Phy. Lett. 70 (1997) 3299–3301.
[4] M.A. Benedict, S.A. Sherif, M. Schroeder, D.G. Beers, Int. J. Refrig. 74 (2017) 576–583.
[5] C.B. Zimm, A. Sternberg, A.G. Jastrab, A.M. Boeder, L.M. Lawton, J.J. Chell, Rotating Bed Magnetic Refrigeration Apparatus, US, Patent No. 6526759, 2003.
[6] N. Hirano, S. Nagaya, M. Takahashi, T. Kuriyama, K. Ito, S. Nomura, AIP Conf. Proc. 613 (2002) 1027–1034.
[7] P. Clot, D. Viallet, F. Allab, A. Kedous-Lebouc, J.M. Fournier, J.P. Yonnet, IEEE Trans. Magn. 39 (2003) 3349–3351.
[8] X.N. He, M.Q. Gong, H. Zhang, W. Dai, J. Shen, J.F. Wu, Int. J. Refrig. 36 (2013) 1465–1471.
[9] M.A. Richard, A.M. Rowe, R. Chahine, J. Appl. Phys. 95 (2004) 2146–2150.
[10] J. Yu, Haier's Newest Prototype Is the Future of Refrigeration, http://refrigerators.reviewed.com/features/haiers-prototype-is-the-future-of-refrigeration, January 9, 2015.
[11] M. Irving, Magnetic Fridge Eliminates Gases, Drastically Reduces Energy Use, https://newatlas.com/cooltech-commercial-magnetic-cooling/43874/, June 15, 2016.
[12] K.A. Gschneidner Jr., V.K. Pecharsky, Annu. Rev. Mater. Sci. 30 (2000) 387–429.
[13] H.X. Zheng, W. Wang, S.C. Xue, Q.J. Zhai, J. Frenzel, Z.P. Luo, Acta Mater. 61 (2013) 4648–4656.
[14] S.T. Feng, Y. Fang, Q.J. Zhai, Z.P. Luo, H.X. Zheng, J. Cryst. Growth 45 (2016) 83–87.
[15] N.K. Sun, Z.X. Ren, L.H. Shen, J. Guo, P.Z. Si, J. Alloys Compd. 690 (2017) 598–603.
[16] J. Liu, C. He, M.X. Zhang, A.R. Yan, Acta Mater. 118 (2016) 44–53.
[17] K. Niitsu, R. Kainuma, Intermetallics 20 (2012) 160–169.
[18] I.A. Radulov, K.P. Skokov, D.Y. Karpenkov, T. Gottschall, O. Gutfleisch, J. Magn. Magn. Mater. 396 (2015) 228–236.
[19] W. Imamura, A.A. Coelho, V.L. Kupfer, A.M.G. Carvalho, J.G. Zago, A.W. Rinaldi, S.L. Favaro, C.S. Alves, J. Magn. Magn. Mater. 425 (2017) 65–71.
[20] M.K. Han, G.J. Miller, Inorg. Chem. 47 (2007) 515–528.
[21] B.G. Shen, J.R. Sun, F.X. Hu, H.W. Zhang, Z.H. Cheng, Adv. Mater. 21 (2009) 4545–4564.
[22] B. Kaeswurm, A. Barcza, M. Vögler, P.T. Geiger, M. Katter, O. Gutfleisch, L.F. Cohen, J. Alloys Compd. 697 (2017) 427–433.
[23] X. Feng, J.K. Qiu, Y.J. Ma, J.F. Lei, Y.Y. Cui, X.H. Wu, R. Yang, J. Mater, Sci. Technol. 32 (2016) 363–371.
[24] M.X. Zhang, J. Liu, C. He, A.R. Yan, Mater. Lett. 134 (2014) 87–90.
[25] S. Fujieda, K. Fukamichi, S. Suzuki, J. Alloys Compd. 566 (2013) 196–200.
[26] O. Kubaschewski, in: T.B. Massalski (Ed.), Binary Phase Diagrams, 2nd ed., ASM International, The Netherlands, 1990, p. 1771.
[27] J. Liu, J.D. Moore, K.P. Skokov, M. Krautz, K. Löwe, A. Barcza, M. Katter, O. Gutfleisch, Scr. Mater. 67 (2012) 584–589.
[28] X. Chen, Y.G. Chen, Y.B. Tang, J. Alloys Compd. 509 (2011) 8534–8541.
[29] S. Fu, Y. Long, Y.Y. Sun, J. Hu, Intermetallics 39 (2013) 79–83.
[30] J. Liu, M. Krautz, K. Skokov, T.G. Woodcock, O. Gutfleisch, Acta Mater. 59 (2011) 3602–3611.
[31] P. Shamba, R. Zeng, J.L. Wang, S.J. Campbell, S.X. Dou, J. Magn. Magn. Mater. 331 (2013) 102–108.
[32] H. Zhang, Y. Long, Q. Cao, M. Zou, K.A. Gschneidner Jr., V.K. Pecharsky, J. Alloys Compd. 509 (2011) 3746–3750.
[33] A. Arrot, Phys. Rev. 108 (1957) 1394–1396.
[34] A.S. Demuner, A.Y. Takeuchi, E.C. Passamani, J.R. Proveti, C. Larica, E. Favre-Nicolin, A.M. Gomes, J. Magn. Magn. Mater. 321 (2009) 1809–1813.
[35] D.Z. Wu, S.C. Xue, J. Frenzel, G. Eggeler, Q.J. Zhai, H.X. Zheng, Mater. Sci. Eng. A 534 (2012) 568–572.
[36] H.W. Li, Y. Fang, S.T. Feng, Q.J. Zhai, Z.P. Luo, H.X. Zheng, J. Magn. Magn. Mater. 417 (2016) 267–271.
[37] S. Fu, Y. Long, J. Hu, Y.Y. Sun, Mater. Lett. 112 (2013) 149–152.
[38] Y.Y. Shao, J. Liu, M.X. Zhang, A.R. Yan, K.P. Skokov, D.Y. Karpenkov, O. Gutfleisch, Acta Mater. 125 (2017) 506–512.